Diffusion Pore Imaging by Hyperpolarized Xenon-129 Nuclear Magnetic Resonance

Tristan Anselm Kuder,[1,*] Peter Bachert,[1] Johannes Windschuh,[1] and Frederik Bernd Laun[1,2]

[1]*Medical Physics in Radiology, German Cancer Research Center (DKFZ), D-69120 Heidelberg, Germany*

[2]*Quantitative Imaging Based Disease Characterization, German Cancer Research Center (DKFZ), D-69120 Heidelberg, Germany*

(Received 21 January 2013; published 10 July 2013)

While NMR diffusion measurements are widely used to derive parameters indirectly related to the microstructure of biological tissues and porous media, direct imaging of pore shapes would be of high interest. Here we demonstrate experimentally that complexly shaped closed pores can be imaged by diffusion acquisitions. Collecting the signal from the whole sample eliminates the problem of vanishing signal at increasing resolution of conventional NMR imaging. This approach may be used to noninvasively obtain structural information inaccessible so far such as pore or cell shapes, cell density, or axon integrity.

DOI: 10.1103/PhysRevLett.111.028101 PACS numbers: 87.61.−c, 61.43.Gt, 66.30.je, 82.56.Lz

The sizes and shapes of cells or pores are important parameters when studying the structural properties of biological tissues and porous media. Regarding the achievable resolution, which is essential for the investigation of such media, the main limiting factor for conventional nuclear magnetic resonance (NMR) imaging, besides the required gradient strength, is the signal-to-noise ratio (SNR). In principle, NMR diffusion measurements can overcome this limitation by using the signal from a larger sample volume yielding information averaged over all contained cells or pores [1–7]. Therefore, NMR diffusion experiments are extensively used not only in porous media research [2,3], but also in the medical field to gain insight into the tissue microstructure *in vivo* [4–7]. Usually, parameters indirectly related to the geometrical structure of barriers confining the diffusion process of the water molecules in tissue are obtained from these measurements, such as the diffusion coefficient and measures characterizing diffusion anisotropy. In the human brain, for example, these parameters can be used to characterize diseases like stroke [8,9] or to investigate the connectivity of brain regions by reconstructing white matter tracts [10,11]. However, direct imaging of the underlying microstructure would be desirable, since it would enable the direct extraction of parameters such as cell size, pore size, and cell shape. For a long time, this aim seemed unaccomplishable because only the magnitude of the pore form factor could be measured, but the phase information was lost [3,12]. Recently, we theoretically proposed an approach to preserve the phase information [13]. In this article, we demonstrate experimentally that the exact geometry of arbitrary closed pores can be obtained from NMR diffusion measurements. This may enable the direct diffusion-based imaging of porous structures at a largely increased SNR compared to conventional NMR imaging.

In NMR diffusion measurements [14,15], to detect the Brownian motion of diffusing spins, the static magnetic field B_0 is modified by a time-dependent field gradient profile $\mathbf{G}(t)$, which fulfils $\int_0^T dt\,\mathbf{G}(t) = 0$ with the total gradient duration T resulting in the field strength $B(t) = B_0 + \mathbf{G}(t)\cdot\mathbf{x}(t)$ for a particle at position $\mathbf{x}(t)$. The signal attenuation due to the diffusion-weighting gradients is given by $S = \langle\exp(i\phi)\rangle$, where $\langle\cdot\rangle$ denotes the average over all possible random paths, and $\phi = -\gamma\int_0^T dt\,\mathbf{G}(t)\cdot\mathbf{x}(t)$ is the phase accumulated in a rotating frame of reference during the random walk $\mathbf{x}(t)$ (gyromagnetic ratio γ).

To gain information about diffusion restrictions, a particularly useful technique is q-space imaging [3,16,17]. Here, two short gradient pulses of duration δ are applied at $t=0$ and $t=T-\delta$ with the gradient vectors $\mathbf{G}$ and $-\mathbf{G}$. It is assumed that the diffusive motion during δ can be neglected. Defining the q value $\mathbf{q} = \gamma\delta\mathbf{G}$ and the pore space function $\rho(\mathbf{x})$, which equals 1 inside the pore and is 0 outside, and assuming that T is sufficiently long so that the correlations between the starting position $\mathbf{x}_1 = \mathbf{x}(0)$ and the final position $\mathbf{x}_2 = \mathbf{x}(T)$ vanish, the signal attenuation becomes

$$\begin{aligned} S_2(\mathbf{q}) &= \langle e^{i\mathbf{q}\cdot(\mathbf{x}_2-\mathbf{x}_1)}\rangle \\ &= \frac{1}{V^2}\int_\Omega d\mathbf{x}_2\rho(\mathbf{x}_2)e^{i\mathbf{q}\cdot\mathbf{x}_2}\int_\Omega d\mathbf{x}_1\rho(\mathbf{x}_1)e^{-i\mathbf{q}\cdot\mathbf{x}_1} \\ &= \frac{1}{V^2}|\tilde{\rho}(\mathbf{q})|^2. \end{aligned} \tag{1}$$

$\tilde{\rho}(\mathbf{q})$ symbolizes the Fourier transform (FT) of $\rho(\mathbf{x})$, V is the pore volume, and Ω is the domain containing the pore. Thus, in analogy to diffraction experiments, the magnitude can be observed, but the inverse FT cannot be calculated due to the missing phase information.

Our approach [13], which we demonstrate experimentally here, uses a combination of a long and a short gradient pulse [Fig. 1(a), gradient shape 1] resulting in the gradient profile $\mathbf{G}(t) = \mathbf{G}_1 = -(\delta_2/\delta_1)\mathbf{G}_2$ for $0 \le t \le \delta_1$ and $\mathbf{G}(t) = \mathbf{G}_2$ for $\delta_1 < t \le T$ with the q value $\mathbf{q} = \gamma\delta_2\mathbf{G}_2$ and $\delta_1 + \delta_2 = T$. Consequently, the signal is given by [13,18,19]

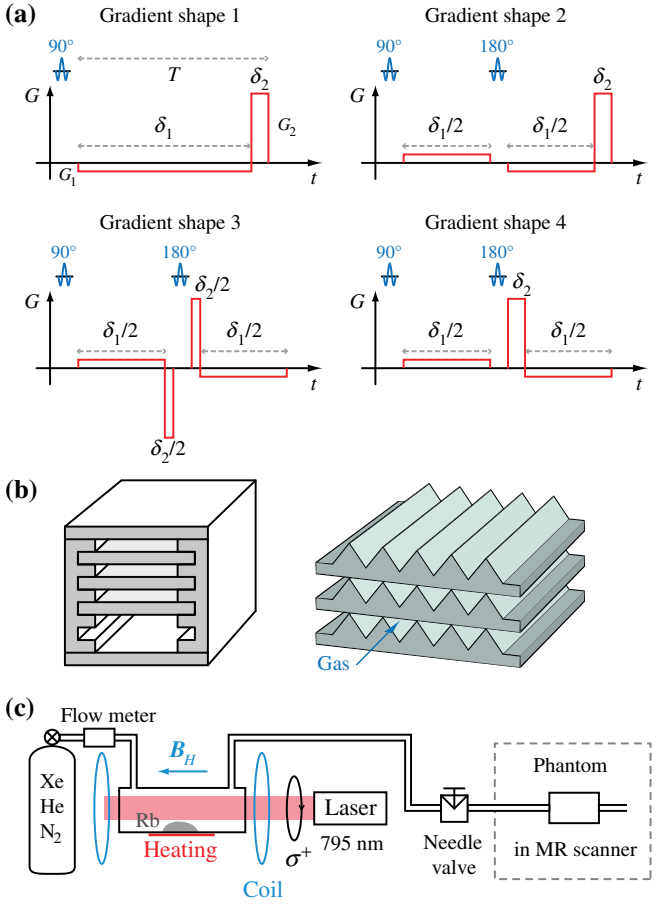

FIG. 1 (color online). Schematic representation of the diffusion-weighting gradient profiles and of the experimental setup. (a) The long-narrow gradient scheme (shape 1) uses a long diffusion-weighting gradient to generate a phase proportional to the pore center of mass and a short imaging gradient. Additionally to the 90° excitation pulse, a 180° refocusing pulse (duration 2.6 ms) can be used to realize a spin echo sequence (shape 2). The gradient timing can be modified (shapes 3, 4). Shapes 2–4 were used for the experiments. (b) Phantoms: parallel plates (distance: 1, 3, and 5 mm) and pores with triangular cross section (equilateral, edge length 3.4 mm). (c) Scheme of the apparatus for generation of hyperpolarized ^{129}Xe gas by spin exchange optical pumping.

$$S(\mathbf{q}) = \left\langle \exp\left[i\mathbf{q} \cdot \left(\frac{1}{\delta_1} \int_0^{\delta_1} d t \mathbf{x}(t) - \frac{1}{\delta_2} \int_{\delta_1}^{T} d t \mathbf{x}(t) \right) \right] \right\rangle = \langle e^{i\mathbf{q}\cdot(\mathbf{x}_{\mathrm{CM},1} - \mathbf{x}_{\mathrm{CM},2})} \rangle. \quad (2)$$

$\mathbf{x}_{\mathrm{CM},1}$ and $\mathbf{x}_{\mathrm{CM},2}$ denote the centers of mass of the particle random walks during application of the gradients $\mathbf{G}_1$ and $\mathbf{G}_2$. Each of these gradients imprints a phase that a particle resting at $\mathbf{x}_{\mathrm{CM},1}$ or $\mathbf{x}_{\mathrm{CM},2}$ would acquire. In the long-time limit (long δ_1), $\mathbf{x}_{\mathrm{CM},1}$ of each random walk during the first gradient converges to the pore center of mass $\mathbf{x}_{\mathrm{CM}}$. Neglecting the diffusive displacements during the short period δ_2, $\mathbf{x}_{\mathrm{CM},2}$ converges to the final point $\mathbf{x}_2$ of the random walk and Eq. (2) becomes

$$S(\mathbf{q}) = \langle e^{i\mathbf{q}\cdot(\mathbf{x}_{\mathrm{CM}} - \mathbf{x}_2)} \rangle = \frac{1}{V} e^{i\mathbf{q}\cdot\mathbf{x}_{\mathrm{CM}}} \int_\Omega d\mathbf{x}_2 \rho(\mathbf{x}_2) e^{-i\mathbf{q}\cdot\mathbf{x}_2} = \frac{1}{V} e^{i\mathbf{q}\cdot\mathbf{x}_{\mathrm{CM}}} \tilde{\rho}(\mathbf{q}). \quad (3)$$

Thus, the phase information is preserved and the inverse FT can be performed to obtain the pore shape. The long gradient results in the factor $e^{i\mathbf{q}\cdot\mathbf{x}_{\mathrm{CM}}}$, which shifts the center of mass of all pores to a common point, while the short gradient acts as an imaging gradient. Consequently, in a medium with many similar pores, all pores contribute to one reconstructed image and an average pore space function can be measured at a higher SNR compared to conventional NMR imaging.

The actual temporal shape of the gradient pulses is not of essential importance, as long as one short and at least one long gradient pulse are applied [18]. This allows using a spin echo sequence to compensate for the signal loss due to local field inhomogeneities [Fig. 1(a), gradient shape 2]. To demonstrate the influence of the gradient shape on the measured signal, for the experiments presented here, additionally to gradient shape 2, the modified gradient shapes 3 and 4 were used.

Experiments were performed using gas filled phantoms containing parallel plates and pores of triangular shape [Fig. 1(b)]. For the experimental demonstration, using gas diffusion is advantageous over water diffusion since the diffusion coefficient is several orders of magnitude larger and thus the long-time limit can be reached in pores on the millimeter scale, which are easy to realize in phantoms. Despite the high diffusion coefficient, the maximum gradient amplitude of a clinical MR scanner was sufficient. Because of the low NMR signal of thermally polarized gases, hyperpolarized ^{129}Xe gas was used, which was generated by spin exchange optical pumping (SEOP) [20–22]. For technical reasons [20], a mixture of helium, nitrogen, and xenon gas was employed, which was transferred by continuous flow to a pumping cell, where it was mixed with rubidium vapor [Fig. 1(c)]. By laser optical pumping, a high electron-spin polarization of the rubidium atoms was generated, which was transferred to the ^{129}Xe nuclear spin ensemble by spin exchange collisions. The hyperpolarized gas was then used for the diffusion measurements in the MR scanner (for technical details see the Supplemental Material [23]).

Figure 2 shows the signal acquired using one gradient direction [gradient shape 3 in Fig. 1(a)] orthogonal to parallel plates as well as the inverse FT for different durations δ_1 of the long gradients. The measured signal and its FT (dots) are in good agreement with the simulation of the diffusion process (solid lines), where the Bloch-Torrey equation was solved numerically using a matrix approach [12,24]. Because of the symmetry of the slits, the imaginary part of the signal is zero [18,25,26]. However, contrary to q-space imaging, the negative signal values now allow the reconstruction of the pore space

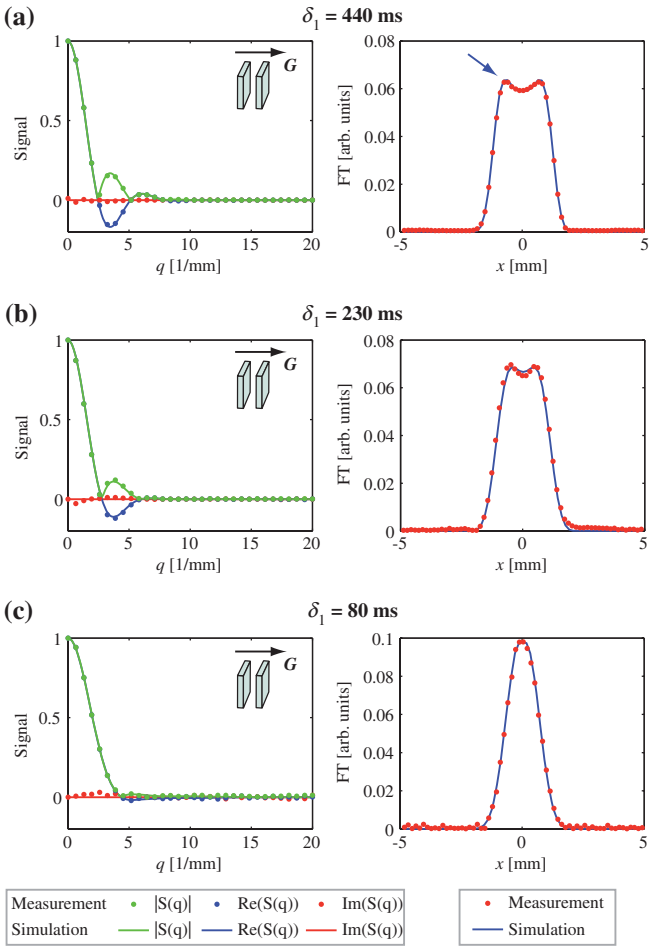

FIG. 2 (color). Measurement results for parallel plates for different durations δ_1 of the long gradient. The measured signals (dots) are in good agreement with the simulation (solid lines) of the diffusion process for the parallel plate phantom (distance 3 mm, 10 slits, $\delta_2 = 7$ ms, free diffusion coefficient $D_0 = 37\,000\ \mu\text{m}^2/\text{ms}$, gradient shape 3). The absolute value of the FT of the signal on the right side clearly shows the single-slit function (averaged over all slits) for the longest diffusion time (a, $\delta_1 = 440$ ms). The edge enhancement effect is clearly visible (blue arrow). For shorter diffusion times, the information about the pore shape gradually vanishes (b), (c).

function. For $\delta_1 = 440$ ms, the FT of the oscillating signal clearly shows the single-slit function, which comprises the signal of all slits in the phantom. Two deviations from the ideal rectangular single-slit function owing to the finite gradient durations can be observed, which were not considered in Eq. (3). The finite δ_1 causes a blurred $\mathbf{x}_{\text{CM},1}$ [Eq. (2)] and a finite slope at the edges. Since δ_2 is not infinitesimal, the edge enhancement effect [18,27] can be observed [Fig. 2(a), blue arrow]: $\mathbf{x}_{\text{CM},2}$ deviates from the trajectory end point $\mathbf{x}_2$ and thus the signal is effectively pushed away from the domain edges yielding an increased signal near the boundaries. For shorter δ_1 [Figs. 2(b) and 2(c)], the distribution of $\mathbf{x}_{\text{CM},1}$ gradually broadens. Consequently, for $\delta_1 = 80$ ms, the signal oscillations and the pore shape information are mostly lost, which emphasizes the importance of reaching the long-time limit.

Figure 3 demonstrates the possibility to image an average pore space function using two different plate distances in a single phantom. The contributions of different pore sizes can be clearly observed. The finite gradient durations cause deviations from a superposition of a narrow and a wide rectangular function.

The measurements of equilateral triangular pores in Fig. 4 exhibit good agreement with the simulations. Since this domain is not point symmetric [18,26], nonzero imaginary parts occur for the vertical gradient direction (arrows). Thus, the full phase information is obtained, which is mandatory to reconstruct arbitrary pores shapes. The sawtooth shaped FT in Fig. 4(a) corresponds to the expected projection of the pore on the gradient direction. The need to use a long-narrow gradient scheme is demonstrated in Figs. 4(b) and 4(c). If the long-narrow requirement is violated, the information about the pore shape is gradually lost. For the horizontal gradient direction [Fig. 4(d)], the signal is real since there exists a symmetry plane orthogonal to the gradient vector.

Figure 5(a) shows results of pore imaging measurements for the phantom with 170 triangular domains. The data were acquired radially with 19 gradient directions and 15 q values using gradient shape 2. The images were calculated by applying a Radon transform to the Fourier transform of the individual spokes. The triangle is clearly visible and in very good agreement with the simulations. All pores in the phantom contribute to one average pore image. For shorter δ_1, the image is blurred due to the broadening of the $\mathbf{x}_{\text{CM},1}$

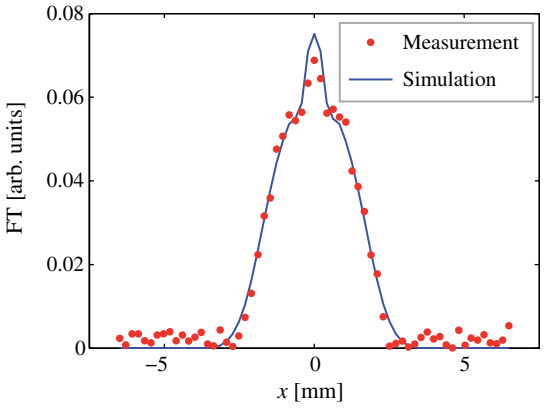

FIG. 3 (color online). Combination of different plate distances in one phantom yielding an average pore shape. The measured and simulated absolute values of the FT for a phantom with different plate distances (six 5-mm slits and two 1-mm slits) show a superposition of the two pore shapes ($\delta_1 = 440$ ms, $\delta_2 = 5.2$ ms, gradient shape 3, maximum q value $q_{\text{max}} = 15\ \text{mm}^{-1}$). Small differences between measurement and simulation regarding the contributions of the two different pore sizes can be attributed to variations of the gas polarization in the two regions.

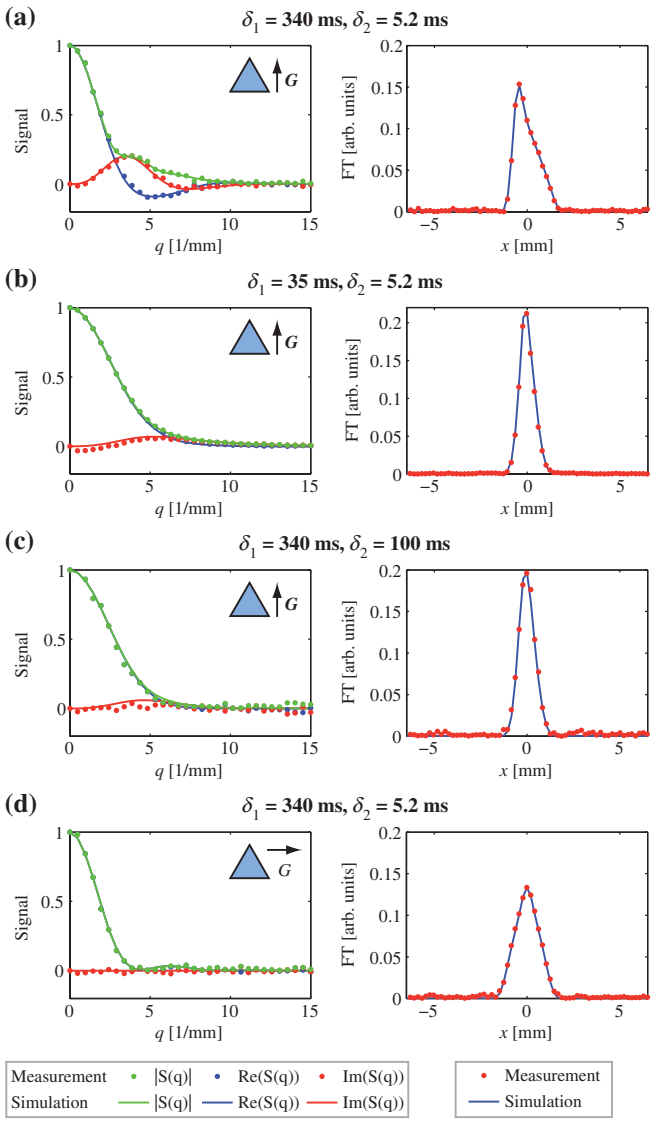

FIG. 4 (color). Experimental results for the equilateral triangular pore shape for single gradient directions. (a) For the vertical gradient direction (arrow), a complex signal arises since there is no mirror plane orthogonal to the gradient direction. The absolute value of the FT of the signal (right side) yields the projection of the pore shape on the gradient direction. (b) A relatively short first gradient or, (c) a long second gradient suppresses the oscillations and the pore shape is lost, because the preconditions of equation (3) are not met. (d) For the horizontal gradient direction, the FT again yields the projection of the pore shape (Parameters: edge length $L = 3.4$ mm, gradient shape 3, 10 plates each with 17 triangular cutouts).

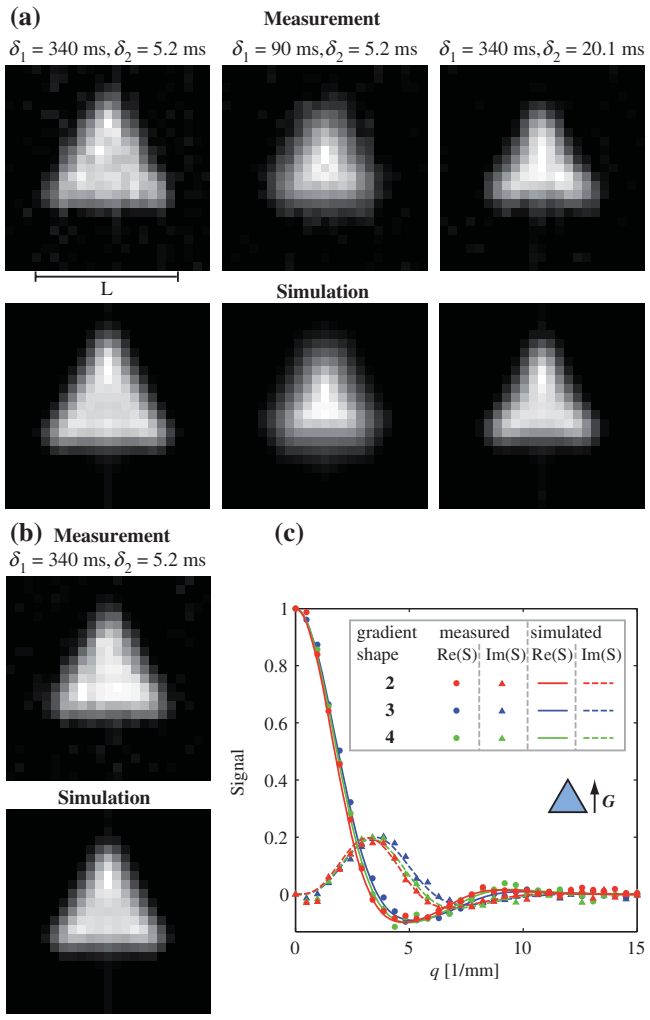

FIG. 5 (color). Pore imaging results for triangular domains. (a) Measurements and simulations for different diffusion times and durations of the short gradient for gradient shape 2 (radial acquisitions with 15 q values for each of the 19 directions, $q_{max} = 15\,\mathrm{mm}^{-1}$, edge length $L = 3.4$ mm). All triangular pores in the phantom contribute to one image and thus the SNR limitation of conventional NMR imaging is lifted. (b) Pore images can also be acquired using gradient shape 3. (c) The choice of the gradient shape has a small influence on the signal, which can be reproduced by the simulations ($\delta_1 = 340$ ms, $\delta_2 = 5.2$ ms).

distribution; because of the edge enhancement effect, the triangle appears shrunk for prolonged δ_2. For comparison, Fig. 5(b) shows pore images measured and simulated for gradient shape 3. Figure 5(c) depicts a comparison of the influence of the gradient shapes. Small differences between the measured signals occur, which can be reproduced remarkably well by the simulation of the diffusion process. Consequently, the gradient shape can be optimized for applications. For example, gradient shape 3 could be used to reduce imaging artifacts caused by concomitant magnetic fields [28].

In conclusion, we have demonstrated experimentally that the proposed new form of diffusion-based magnetic resonance imaging can reveal the average shape of arbitrary closed pores in a volume with many pores, which mainly overcomes the SNR limitation of conventional NMR imaging [29]. Thus, average pore shapes could be imaged with a resolution far beyond the range currently accessible to NMR techniques. Regarding actual applications, namely to image cells, several complications would have to be addressed. Imaging axons demands submicrometer resolution. Hence,

very strong gradients would be required, which are not available on clinical scanners. The membranes of cells are semipermeable, while the individual pores in porous media may be interconnected. This may violate the basic assumptions of the method presented here. Additionally, extracellular free water will add a background signal, which, however, may drop considerably faster with increasing q value than the signal of water confined in pores. Thus, it may be suppressed fairly well at relatively low q values.

In the case of distributions of pore size, shape, and orientation, only an average pore image will be reconstructed, which may be used to extract information about the distribution of pore sizes in the sample, but details of the pore shapes will be obscured. The precondition to obtain an average image is, however, that the long-narrow criterion is fulfilled for all considered pore sizes and shapes implying constraints on the minimum relaxation times and the gradient strength. Furthermore, susceptibility-induced gradients may be problematic. Several limitations were discussed in detail recently [18].

Diffusion pore imaging is currently a quickly evolving field of research, which is now in the stage of first experimental verifications. Very recently, for cylindrical capillaries and the long-narrow gradient scheme, initial pore images with micron resolution have been presented [30,31]. A different approach to diffusion pore imaging for point-symmetric pores [32,33], which can be generalized to arbitrary shapes [26], was demonstrated by application to capillaries. For point-symmetric domains, pore imaging techniques rely on the sign of $\tilde{\rho}(\mathbf{q})$, but the imaginary part vanishes. Our results show the possibility of acquiring the phase information of $\tilde{\rho}(\mathbf{q})$ and verifying experimentally that arbitrary non-point-symmetric pores can be imaged without relying on assumptions. For practical applications, the above mentioned complications would have to be overcome. Besides imaging of porous media such as oil-containing rocks or cement, gaining information about cells in biological tissues, e.g., retrieving parameters usually derived from histology such as tumor cellularity or axon integrity, could be a promising field of application.

We thank Guido Antweiler for valuable technical contributions to the hyperpolarization setup, Reiner Umathum for the construction and test of the transmit-receive switch and preamplifier, Moritz Berger for building the ^{129}Xe NMR coil, and Florian Meise for setting up the coil configuration files. We acknowledge helpful discussions with Bram Stieltjes. Financial support by the DFG (Grant No. LA 2804/2-1) is gratefully acknowledged.

*To whom all correspondence should be addressed.
t.kuder@dkfz.de

[1] P. T. Callaghan, *Principles of Nuclear Magnetic Resonance Microscopy* (Oxford University Press, Oxford, 1991).
[2] P. N. Sen, Concepts Magn. Reson. Part A **23A**, 1 (2004).
[3] P. T. Callaghan, A. Coy, D. MacGowan, K. J. Packer, and F. O. Zelaya, Nature (London) **351**, 467 (1991).
[4] D. Le Bihan, J.-F. Mangin, C. Poupon, C. A. Clark, S. Pappata, N. Molko, and H. Chabriat, J. Magn. Reson. Imag. **13**, 534 (2001).
[5] D. Le Bihan, Nat. Rev. Neurosci. **4**, 469 (2003).
[6] P. J. Basser, NMR Biomed. **8**, 333 (1995).
[7] D. S. Novikov, E. Fieremans, J. H. Jensen, and J. A. Helpern, Nat. Phys. **7**, 508 (2011).
[8] S. Warach, D. Chien, W. Li, M. Ronthal, and R. R. Edelman, Neurology **42**, 1717 (1992).
[9] A. G. Sorensen *et al.*, Radiology **199**, 391 (1996).
[10] D. K. Jones, *Diffusion MRI* (Oxford University Press, Oxford, 2011).
[11] S. Mori and P. C. M. van Zijl, NMR Biomed. **15**, 468 (2002).
[12] D. S. Grebenkov, Rev. Mod. Phys. **79**, 1077 (2007).
[13] F. B. Laun, T. A. Kuder, W. Semmler, and B. Stieltjes, Phys. Rev. Lett. **107**, 048102 (2011).
[14] E. O. Stejskal and J. E. Tanner, J. Chem. Phys. **42**, 288 (1965).
[15] E. O. Stejskal, J. Chem. Phys. **43**, 3597 (1965).
[16] P. T. Callaghan, D. Macgowan, K. J. Packer, and F. O. Zelaya, J. Magn. Reson. **90**, 177 (1990).
[17] D. G. Cory and A. N. Garroway, Magn. Reson. Med. **14**, 435 (1990).
[18] F. B. Laun, T. A. Kuder, A. Wetscherek, B. Stieltjes, and W. Semmler, Phys. Rev. E **86**, 021906 (2012).
[19] P. P. Mitra and B. I. Halperin, J. Magn. Reson., Ser. A **113**, 94 (1995).
[20] T. G. Walker and W. Happer, Rev. Mod. Phys. **69**, 629 (1997).
[21] A. M. Oros and N. J. Shah, Phys. Med. Biol. **49**, R105 (2004).
[22] N. J. Shah, T. Ünlü, H.-P. Wegener, H. Halling, K. Zilles, and S. Appelt, NMR Biomed. **13**, 214 (2000).
[23] See Supplemental Material at http://link.aps.org/supplemental/10.1103/PhysRevLett.111.028101 for technical details of materials and methods.
[24] S. Axelrod and P. N. Sen, J. Chem. Phys. **114**, 6878 (2001).
[25] E. Özarslan and P. J. Basser, J. Magn. Reson. **188**, 285 (2007).
[26] T. A. Kuder and F. B. Laun, Magn. Reson. Med., doi:10.1002/mrm.24515 (2012).
[27] T. M. De Swiet, J. Magn. Reson., Ser. B **109**, 12 (1995).
[28] M. A. Bernstein, X. J. Zhou, J. A. Polzin, K. F. King, A. Ganin, N. J. Pelc, and G. H. Glover, Magn. Reson. Med. **39**, 300 (1998).
[29] T. A. Kuder and F. B. Laun, 11th International Bologna Conference on Magnetic Resonance in Porous Media, Guildford, UK, 2012, Talk O21.
[30] S. A. Hertel, M. Hunter, and P. Galvosas, 11th International Bologna Conference on Magnetic Resonance in Porous Media, Guildford, UK, 2012, Poster 6.8.
[31] S. A. Hertel, M. Hunter, and P. Galvosas, Phys. Rev. E **87**, 030802 (2013).
[32] N. Shemesh, C. F. Westin, and Y. Cohen, Phys. Rev. Lett. **108**, 058103 (2012).
[33] V. G. Kiselev and D. S. Novikov, Phys. Rev. Lett. **110**, 109801 (2013).